Research Article Vol. 2, No. 7 / 15 Jul 2023 / Optics Continuum 1735
OPTICS CONTINUUM

Focusing characteristic change and processing characteristic evaluation of femtosecond-to-picosecond pulse lasers above the air ionization threshold

ITSUKI NISHIBATA,[1,*] NOBUHIKO NAKANII,[2] AND TOMOKAZU SANO[1]

[1] *Division of Materials and Manufacturing Science, Graduate School of Engineering, Osaka University, Suita, Osaka 565-0871, Japan*
[2] *Kansai Institute for Photon Science (KPSI), National Institutes for Quantum Science and Technology (QST), 8-1-7 Umemidai, Kizugawa, Kyoto 619-0215, Japan*
[*] *i.nishibata@mapse.eng.osaka-u.ac.jp*

Abstract: The utilization of ultrashort pulse lasers surpassing the air ionization threshold may result in detrimental focusing due to nonlinear optical phenomena. In the context of ultrashort pulse laser processing, alterations in focusing characteristics can lead to reduced processing efficiency and quality. In this study, numerical simulations were conducted to visualize the focusing characteristics across pulse durations ranging from femtoseconds to picoseconds. The distribution of fluence and the position of maximum focus during laser focusing are found to be dependent on the pulse duration, and correction of the irradiation position is crucial for achieving proper processing. The intensity and fluence achieved under high numerical aperture (NA) conditions are determined by the combination of NA and pulse duration. These findings are crucial in selecting optimal laser conditions and achieving optimal control of the processing position in high-energy laser processing applications.

1. Introduction

Ultrashort pulse laser processing is utilized for precise processing of metals and other materials [1,2]. Commercialized, stable, high-output laser systems now allow for laser processing at high repetition frequencies and high pulse energies, which is expected to benefit technologies utilizing substantial pulse energies, such as laser peening [3]. The use of pulse energies in the magnitude of millijoules has garnered attention as a method of achieving sufficient impact force for laser peening, even in air. Ultrashort pulse lasers, with pulse energies over a few microjoules, exhibit high laser intensity when focused by a lens with a focal length of several tens of millimeters, resulting in nonlinear optical phenomena, such as the optical Kerr effect [4] and ionization. These phenomena affect laser propagation in both air and transparent materials [5,6], and alter focusing characteristics, such as fluence distribution, resulting in reduced processing efficiency and quality [7–10]. Understanding the focusing characteristics is especially significant, as nonlinear optical effects become more pronounced when large pulse energies are utilized.

Simulating ultrashort pulse laser propagation above the air ionization threshold can be achieved through the use of nonlinear propagation calculations [11,12]. These calculations involve accounting for both nonlinear optical effects, such as the optical Kerr effect and air plasma, and linear effects, such as diffraction and dispersion, through the numerical solution of the nonlinear Schrödinger equation. The generation of air plasma is accomplished by solving the rate equation for electrons, which incorporates both laser-induced ionization and impact ionization. Research into air ionization through laser fields has been ongoing since the 1960s, and various methods for calculating ionization rates have been reported, with good agreement with experimental results

#496411 https://doi.org/10.1364/OPTCON.496411
Journal © 2023 Received 24 May 2023; revised 5 Jul 2023; accepted 5 Jul 2023; published 15 Jul 2023

[13,14]. These simulations have successfully replicated a specific phenomenon of ultrashort laser pulse propagation, known as laser filamentation, where the focal length is on the order of meters [15–18]. In the field of filamentation, it is widely acknowledged that air ionization plays a dominant role in determining the focusing characteristics of ultrashort pulse lasers with short focal lengths and high numerical apertures (NAs) [19–21]. It is also understood that longer pulse durations result in higher attainable fluence [22,23]. Given that the achieved fluence is a critical metric in laser processing, dictating the processing limits, a thorough comprehension of focusing characteristics in the femtosecond-to-picosecond range is of utmost importance. Consequently, nonlinear propagation calculations are expected to be extensively employed in the realm of ultrashort pulse laser processing.

Several studies have indeed been reported in order to predict processing outcomes from nonlinear propagation calculations [24–27]. However, the pulse energies in the aforementioned examples are limited to a range of a few μJ to 1 mJ, with a narrow spectrum of pulse durations, such as 43 fs or 150 fs. Moreover, these studies have primarily focused on processing at the focal point, with no attention given to processing by altering the position of the laser irradiation. The position where the best processing can be done should fluctuate depending on the divergence of the laser. In the context of ultrashort pulse laser processing, such as laser peening, it is desirable to expand the visualization of the focusing characteristics over a broader range of pulse durations, encompassing picosecond pulses, at a pulse energy of approximately 1 mJ.

The aim of this study was to employ nonlinear propagation calculations utilizing femtosecond to picosecond pulse durations in order to discern the focusing characteristics in ultrashort pulse laser processing employing pulse energies around millijoule. The fluence distribution in proximity to the focal point, which is the most crucial aspect of laser processing, was calculated and compared with experimental results. The impact of nonlinear optical phenomena on the focusing characteristics was assessed, and the alteration of the focusing characteristics with pulse duration was evaluated. Comprehension of the dominant nonlinear optical phenomena and visualization of focusing characteristics are crucial methods for optimizing laser processing conditions and predicting processing outcomes.

2. Methods

2.1. Experimental methods

Ultrashort pulse laser processing was carried out under conditions surpassing the air ionization threshold. As illustrated in Fig. 1(a), the laser beam was focused onto the metal using a plano-convex lens having a focal length of 71.54 mm, and was irradiated at each position eight times in 0.25 mm increments ranging from 3.0 mm upstream to 1.5 mm downstream of the focal point, utilizing a stage that moved in the Z direction. The laser conditions were as follows: the wavelength was 1028 nm, the beam diameter was 3.5 mm, and the pulse energy was 0.85 mJ after passing through the lens. The pulse durations were τ =180 fs, 1 ps, and 4 ps ($\tau_{FWHM} = \tau\sqrt{2ln2}$ =212 fs, 1.18 ps, 4.72 ps).

To assess the pulse duration-dependent laser focusing properties, we obtained the laser irradiation area and ablation area. As shown in Fig. 1(b), the transition of laser irradiation area was measured by scanning electron microscope (SEM) to measure the generation of laser-induced periodic surface structures (LIPSS). Also, shown in Fig. 1(c), the transition of ablation area was measured by laser microscope to determine a removal area of 0.5 μm per 8 shots.

2.2. Numerical simulation methods

The method employed for calculating nonlinear pulse laser propagation utilized the nonlinear Schrödinger equation (NLSE), as expounded in [11]. With an NA of 0.025, it was deemed appropriate to use the NLSE for the calculation, as opposed to the unidirectional pulse propagation

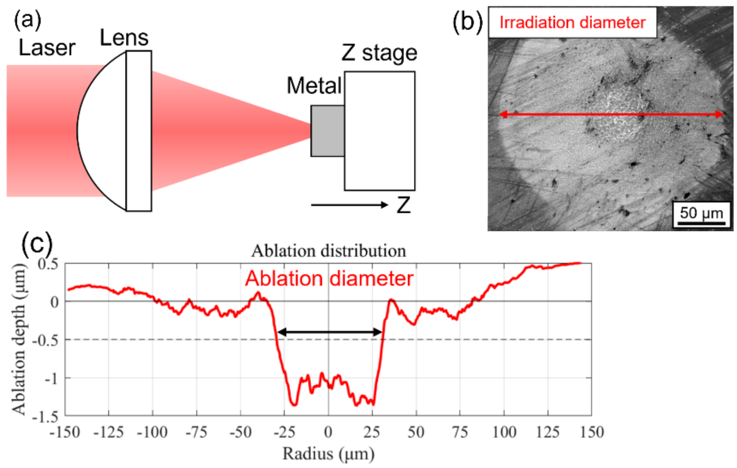

Fig. 1. The experimental setup for laser processing near the focal point. (a) schematic diagram, (b) SEM image showing the laser irradiated area, (c) ablation distribution by laser microscopy.

equation.

$$\frac{\partial \mathcal{E}}{\partial \xi} = \frac{i}{2k_0}\Delta_\perp \mathcal{E} - i\frac{k_0^{(2)}}{2}\frac{\partial^2 \mathcal{E}}{\partial \tau^2} + i\frac{k_0}{n_0}n_2(1-\alpha)I\mathcal{E} + i\frac{k_0}{n_0}n_2\alpha\int_{-\infty}^{t} R_0\, exp[-\Gamma(t-\tau)]$$
$$\times\, sin[\omega_R(t-\tau)]|\mathcal{E}(\tau)|^2 d\tau\mathcal{E} - \frac{1}{2}\frac{\mathrm{W}(I)K\hbar\omega_0(\rho_{nt}-\rho)}{I}\mathcal{E} - \frac{\sigma_{IB}(\omega_0)}{2}(1+i\omega_0\tau_c)\rho\mathcal{E} \quad (1)$$

See the Appendix for the meaning of symbols used in the formula. The first and second terms on the right-hand side correspond to diffraction and dispersion, respectively, while the rest describe the nonlinear optical effects. The third, fourth, fifth, and sixth terms represent the Kerr effect, Raman-Kerr effect, laser-induced ionization, and absorption caused by the electron density in the real part and plasma defocusing in the imaginary part, respectively.

The calculations for air ionization account for both laser ionization and impact ionization. Recombination can be neglected for time scales as short as picoseconds [22]. While Eq. (2) from [11] is a widely used method for impact ionization calculations, it is only applicable when the electron density is sufficiently small and is not appropriate for strong focusing at high pulse energies, such as those used in the present study.

$$\frac{d\rho}{dt} = W(I)(\rho_{nt} - \rho) + \frac{\sigma_{IB}(\omega_0)}{U_m}\rho I \quad (2)$$

Furthermore, in [22], a calculation of impact ionization for picosecond pulses was reported, utilizing the second term on the right-hand side of Eq. (2) as the impact ionization cross section, which depended on the electron temperature and the remaining neutral molecule density. However, this method was unsuitable for calculations of femtosecond pulse laser, as impact ionization occurs instantaneously even if the electron temperature is not sufficiently high. Hence, in the present calculation, we adopted the method presented in [23]. Equations (3) and (4) illustrate this method, which considers the energy distribution of electrons and the time delay, as impact ionization only occurs once the electrons have the requisite energy for impact ionization. Consequently, this method enables calculation for a broad range of pulse durations, including both femtosecond and picosecond pulses.

$$\begin{aligned}\frac{d\rho(\epsilon)}{dt} &= \sum_m [-\nu_m(\epsilon)\rho(\epsilon) + \nu_m(\epsilon + U_m)\rho(\epsilon + U_m)] \\ &+ \delta(\epsilon)\int_0^\infty \nu_m(\epsilon')\rho(\epsilon')d\epsilon' + \delta(\epsilon)W(I)P_m\end{aligned} \tag{3}$$

Here, $\rho(\varepsilon)$ denotes the electron density in energy ε, and m corresponds to either an oxygen or nitrogen molecule. The literature [28] provides the electron impact ionization rate as $\nu_m(\epsilon)$ based on the electron energy. The first term on the right-hand side denotes the reduction of energy ε electrons resulting from impact ionization. The second term signifies the increase in energy ε electrons due to impact ionization. The third term represents the production of secondary electrons with zero energy, as a result of impact ionization. The fourth term indicates the production of zero-energy electrons due to laser ionization. The PPT model was used for laser ionization. In the present study, the modified PPT model was employed, which determines the ionization rate by assigning an appropriate value for the Coulomb potential at a wavelength of 800 nm [29].

We employed the Drude model to describe the amplification of electron energy resulting from inverse Bremsstrahlung.

$$\frac{d\epsilon}{dt} = \frac{1}{2}\frac{e^2E^2}{m}\frac{\nu_{cm}}{\nu_{cm}^2 + \omega_0^2} \tag{4}$$

In this context, the mean free time until collision with a neutral particle, known as τ_c, is utilized as the time constant for calculating the nonlinear propagation of laser filamentation.

The physical properties of nonlinear optical effects have been extensively studied at a wavelength of 800 nm. However, to the best of our knowledge, there is a lack of comprehensive literature available for a wavelength of 1028 nm. Since the Kerr indices at 800 and 1250 nm are within the margin of error [30] and no significant differences exist between 800 and 1028 nm, we have chosen to use the Kerr and Raman-Kerr effect indices of the atmosphere at a wavelength of 800 nm [17,31]. Table 1 displays the physical properties used in this computation.

Table 1. The parameter used in Eq. (1), (3), and (4)

Parameter	Value
n_0: linear refraction index	1.000283
$k_0^{(2)}$: group velocity dispersion	0.2 fs^2/cm [32]
n_2: nonlinear index coefficient	2.9×10^{-19} cm^2/W [31]
α: factor for the proportion of Kerr and Raman-Kerr effects	0.5
Γ^{-1}: molecular response time	70 fs [17]
ω_R: molecular rotational frequency	16 THz [17]
τ_c: electron collision time	350 fs [17]
σ_{IB}: cross section for inverse Bremsstrahlung	9.0×10^{-20} cm^2

We employed a radial-dependent split-step Fourier method [11] to solve the aforementioned equation. Assuming a Gaussian-distributed laser in space-time as initial conditions, we began the calculation with the laser ideally focused 6 mm upstream from the focal point and completed the calculation 4 mm behind the focal point. Table 2 displays the step sizes employed in the calculation, with dr representing the radial step size, dt representing the time step size, and dz representing the propagation step size. As nonlinear optical effects may alter the complex electric field amplitude, the propagation step calculation necessitated a step size small enough to ensure that the change in the electric field amplitude was less than 1% under large ionization conditions.

OPTICS CONTINUUM

The fluence distribution in the propagation direction was calculated by summing up the product of the laser intensity distribution at each time and the time step size. The process described in the paragraphs above is coded in MATLAB. These calculations were performed on a single CPU (Corei9-11900K, Intel Corp.), taking approximately 120 hours. Ignoring impact ionization, the calculation could be completed within a few hours.

Table 2. Computational dimensions for each pulse duration in the numerical simulations

Pulse duration	dr	dt	dz
180 fs	0.7 µm	2.1 fs	0.6 µm
1 ps	0.7 µm	5.9 fs	1.8 µm
4 ps	1.5 µm	5.9 fs	1.8 µm

3. Results

3.1. Transition of irradiated area and ablation area

Figure 2(a) and (b) present the irradiated and ablated regions, respectively, as determined by measurements. The data for the irradiation area transition were obtained by adding vacuum conditions to the data in reference [10] and adjusting the axes. The ideal fluence distribution, which is symmetrical with respect to the focal point, was observed under vacuum conditions. However, under air conditions, the experimental results indicate upstream divergence in both (a) and (b), which is asymmetric with respect to the focal point. The ablation region transition at 180 fs showed a sharp decrease behind the focal point. In longer pulse duration conditions (4 ps), the ablation area remained relatively unchanged, but divergence was observed in the irradiation area transition. These findings suggest that shorter pulse durations and higher laser intensities cause upstream divergence of laser, which can adversely affect the processing outcomes.

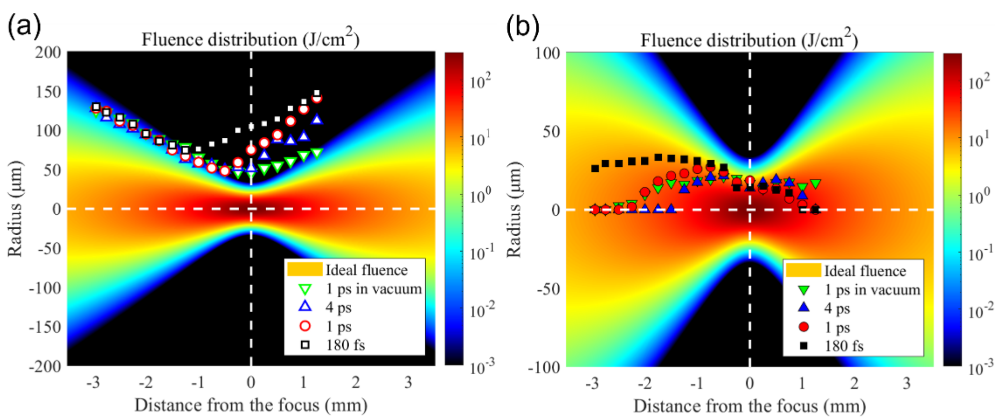

Fig. 2. The ideal fluence distribution and the experimental results for both the irradiated and ablation areas. (a) the transition of the irradiated area, (b) the transition of the ablation area. The color map shows the ideal fluence distribution under vacuum conditions.

3.2. Fluence distribution

In this section, an attempt was made to simulate and validate the divergence of the laser prior to the focal point. The theoretical ideal fluence in a vacuum and the fluence distributions attained via non-linear propagation calculations for each pulse duration condition are displayed in Fig. 3(a)-(d).

OPTICS CONTINUUM

Specifically, the peak fluence was observed to be 30 J/cm^2 for a pulse duration of 180 fs, 100 J/cm^2 for 1 ps, and 250 J/cm^2 for 4 ps, corresponding to approximately 10%, 33%, and 83% of the ideal fluence of 300 J/cm^2, respectively. It is noteworthy that while the achieved fluence increases with pulse duration, it differs from the values previously reported in the literature [22]. This difference in fluence is believed to arise due to the variation in NA. When a pulse duration of 180 fs is employed, the fluence distribution behind the focal point takes on a distinctive shape known as ring formation, in which the center and the periphery are intensified [5].

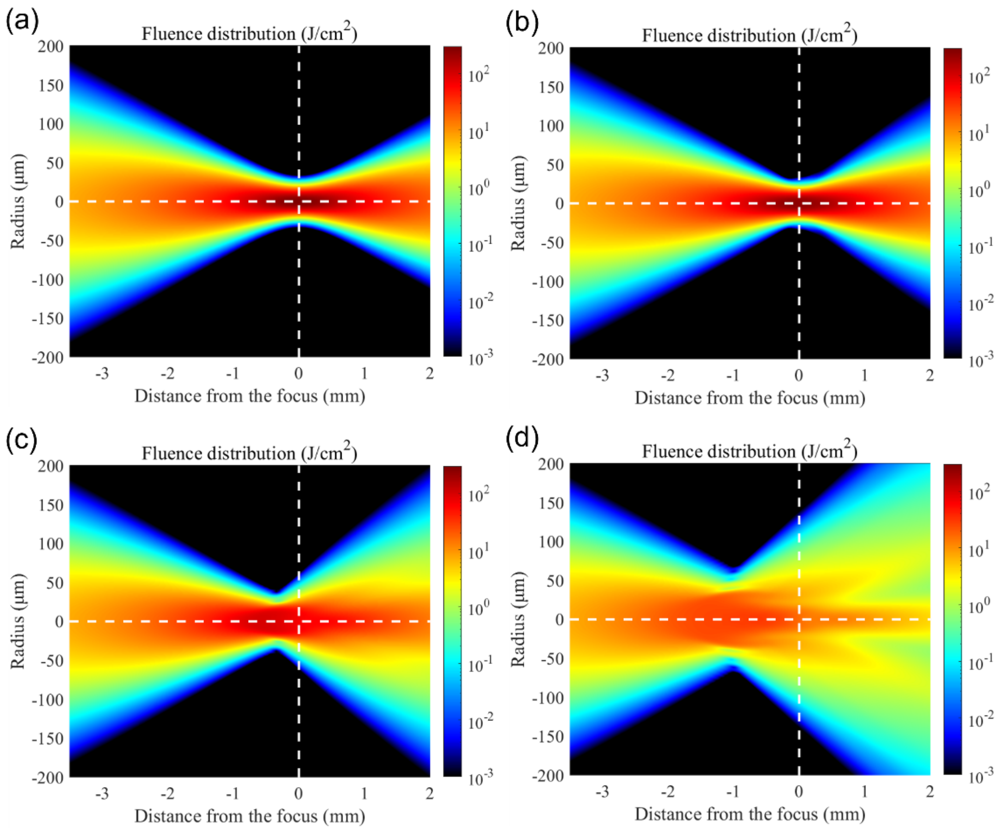

Fig. 3. Fluence distributions calculated by NLSE for each condition; (a) 1ps in vacuum, (b) 4ps, (c) 1 ps, (d) 180 fs.

The computed fluence distribution was subsequently juxtaposed with the experimental outcomes. A line was delineated on the basis of a certain fluence threshold within the computed fluence distribution, and the experimental results were depicted in Fig. 4(a)-(d). The fluence threshold employed in the laser-irradiated zone was standardized at 0.01 J/cm2, regardless of the pulse duration. The fluence threshold for the ablation region was 9 J/cm^2 at 180 fs, 22 J/cm^2 at 1 ps, and 30 J/cm^2 at 4 ps. Additionally, the corresponding threshold lines within the theoretical fluence distribution were illustrated with green dotted lines. The experimental results upstream are consistent with the ideal focal fluence distribution, indicating that the impact of self-focusing caused by the optical Kerr effect is minor, while the dominant factor is divergence caused by plasma. This observation is in line with previous studies [19–21]. The divergence position was replicated with ample precision for the 180 fs and 1 ps pulse duration conditions within the laser-irradiated area. However, the divergence was more restrained under the 4 ps pulse duration condition compared to the results obtained from experimentation. There was a reasonably satisfactory concurrence observed for the transition of the ablation zone across all conditions, although longer pulse duration conditions exhibited a tendency to underestimate the divergence behind the focal point. The capability to predict the ablation area facilitates the selection of processing conditions.

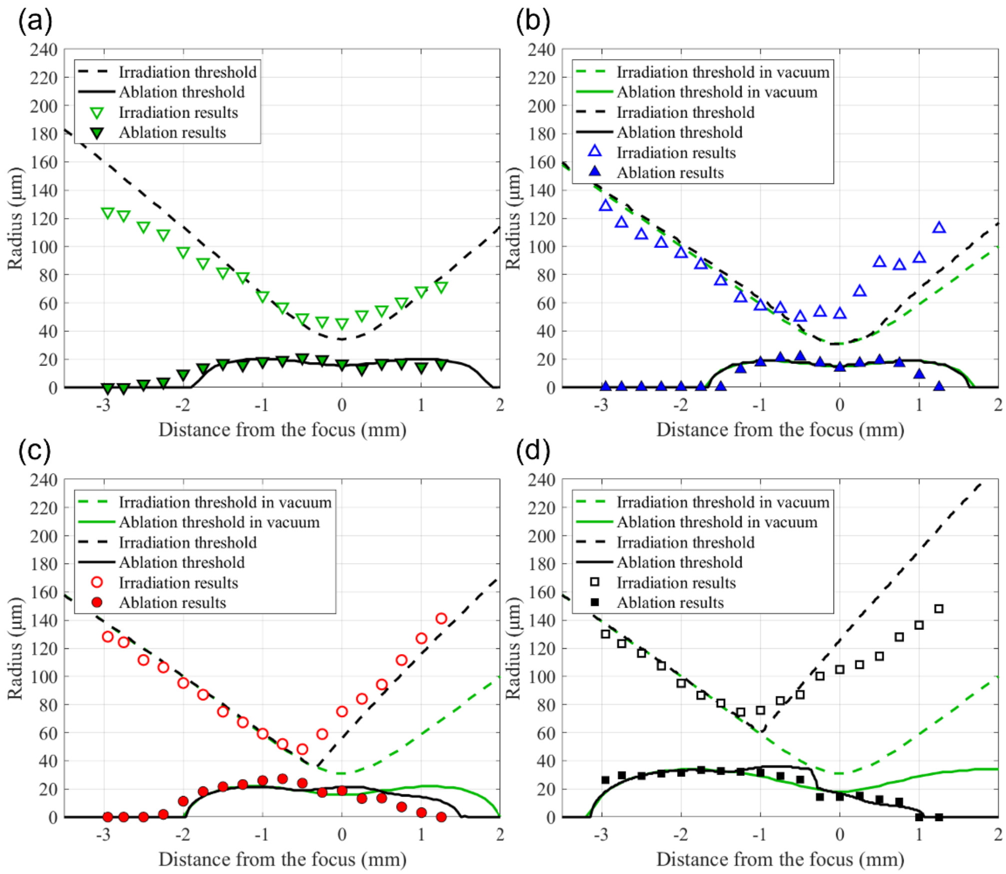

Fig. 4. Comparison of experimental and computed results for transitions in irradiation and ablation areas for each condition; (a) 1ps in vacuum, (b) 4ps, (c) 1 ps, (d) 180 fs.

In the realm of ultrashort pulse laser processing, the proportion of energy utilized for ablation is a crucial metric. As such, the results of the calculation of the total energy within the region where the fluence surpasses the ablation threshold are illustrated in Fig. 5(a)-(d). It is observable that the apex percentage is obtained at the focal point under vacuum conditions. The pulse duration of 4 ps yields scarcely any alteration in the focusing characteristics, hence the percentages are akin to those of vacuum. At a pulse duration of 1 ps, the highest value is achieved at 0.4 mm upstream in contrast to the vacuum focal point, but this value remains unaffected. Consequently, provided the laser irradiation location is appropriately shifted, processing efficiency can be sustained. At 180 fs pulse duration, the peak value is achieved at 1.1 mm upstream, but the value is approximately 7% less than the ideal condition. The movement of the irradiation position is imperative as roughly 90% of the energy is squandered upon irradiation at the focal point. In laser impact processing such as laser peening, the ablation energy is linked to the impact force [33]. Hence, the ability to select the appropriate irradiation position via nonlinear propagation calculation is consequential.

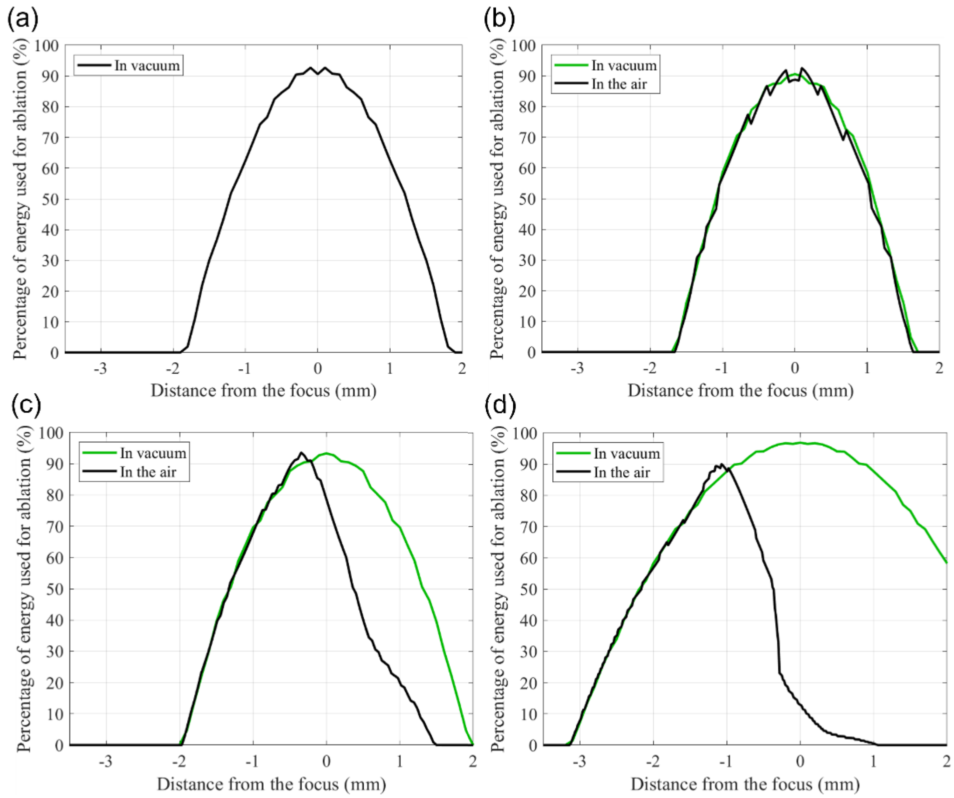

Fig. 5. Percentages of energy used for ablation for each condition; (a) 1ps in vacuum, (b) 4ps, (c) 1 ps, (d) 180 fs.

3.3. Contribution of the optical Kerr effect

Although it is widely acknowledged that laser filamentation is characterized by divergence due to plasma and self-focusing due to the optical Kerr effect, the optical Kerr effect's contribution under the current conditions is negligible. This section provides an account of the optical Kerr effect's contribution to the fluence distribution at 180 fs. The ring-formation fluence distribution with a pulse duration of 180 fs can be explained by the temporal variation of the pulse. As shown in Fig. 6(a), the pulse is split into three parts in the temporal direction so that the energy ratio is approximately equal (31%:38%:31%), and the fluence distribution obtained from each part is output. Figure 6(b)-(d) demonstrates the results of outputting the fluence distribution obtained from each region. During the first region of the pulse, the laser is more focused than 1.0 mm upstream, and the maintenance of high fluence at the beam's center is attributable to this. It is established that region 2, which includes the pulse center, and region 3 behind the pulse are subjected to divergence due to plasma buildup, resulting in upstream divergence. We have set the optical Kerr effect's value to zero ($n_2 = 0$) and the Raman Kerr component to zero (α=0), but have confirmed that these calculations do not alter the results. To summarize, we find that under high NA conditions, the fluence distribution during propagation is characterized by the temporal variation of the pulse due to plasma accumulation.

OPTICS CONTINUUM

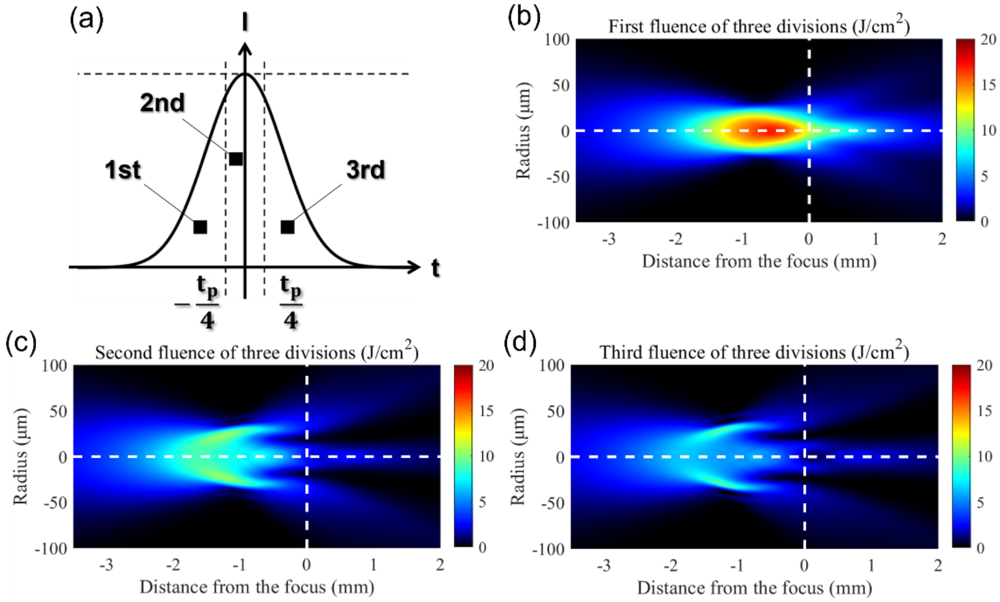

Fig. 6. (a) Schematic diagram illustrating the temporal trisection of the pulse, (b)-(d) the fluence distributions formed from each temporal region.

3.4. Spatio-temporal profiles at specific distances from the focal point

This section presents spatio-temporal profiles at specific distances from the focal point to observe changes associated with 180 fs propagation conditions, which are characterized by pronounced laser divergence. Figure 7 displays the spatio-temporal profile output from 1.5 mm upstream of the focal point to the focal point in 0.5 mm increments. The pulse maintains a Gaussian shape in the spatio-temporal direction at 2.0 mm upstream of the focal point, but distortion begins to occur backward in time of the pulse around 1.5 mm upstream. The distortion is attributed to the accumulation of plasma, which primarily affects the rear of the pulse. At 1.0 mm upstream, the profile distortion also occurs at the pulse center. This can be explained by the fact that the increase in laser intensity associated with focusing causes sufficient plasma accumulation in a short period of time, and the first half of the pulse is also affected by plasma defocusing.

3.5. Plasma generation mechanism

Next, the amount of plasma generation, the dominant nonlinear optical phenomenon in this calculation, is presented. Figure 8(a)–(c) show the free electron density distribution at the end of the calculation for each pulse duration. Figure 8(d)–(f) illustrate the proportion of oxygen ions in the total electron density. The calculated peak electron densities reached 3.5×10^{18} /cm^3 at 4 ps, 4.0×10^{18} /cm^3 at 1 ps, and 2.5×10^{18} /cm^3 at 180 fs. The location and magnitude of plasma generation are significantly dependent on the pulse duration. Furthermore, the proportion of oxygen to nitrogen ions generated in the plasma by the laser is pulse duration-dependent, which is consistent with reference [33] that reported more laser ionization of oxygen molecules with low ionization energy under short pulse duration conditions. With increasing pulse duration, the proportion of nitrogen ions in the plasma also increases, reaching ionization peaks of 75%, 59%, and 39% at 4 ps, 1 ps, and 180 fs, respectively. This increase in nitrogen ions with pulse duration is consistent with reference [22]. As the pulse duration extends beyond picoseconds, impact ionization begins to manifest a few picoseconds after laser ionization, with a greater

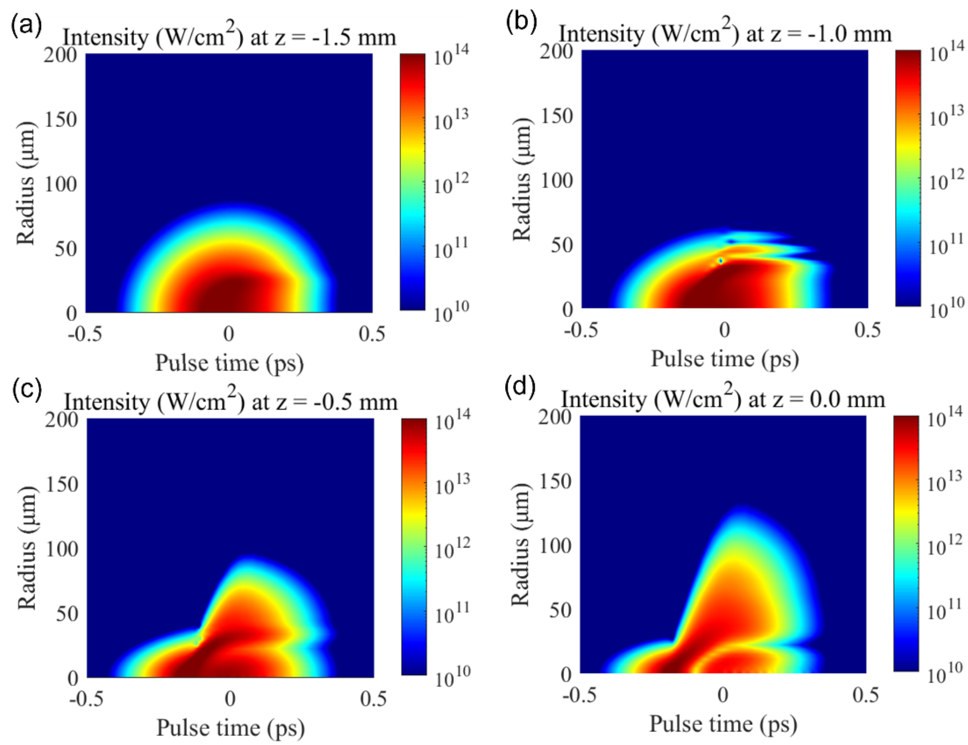

Fig. 7. The laser spatio-temporal profiles at specific distances from upstream to the focal point. (a) -1.5 mm, (b) -1.0 mm, (c) -0.5 mm, and (d) 0.0 mm.

extent observed at 4 ps. As the impact ionization adequately ionizes nitrogen molecules, the degree of nitrogen ionization escalates with longer pulse durations. Figure 9(d) illustrates the ratio of laser ionization volume to the total ionization volume when the respective pulse centers are most focused. Essentially, it serves as an indicator of how the amount of laser ionization influences changes in the focusing characteristics of the pulse center. With a pulse duration of 180 fs, impact ionization comprises below 0.01%. Even with a pulse duration of 4 ps, laser ionization accounts for 91% of the total, while impact ionization remains below 10%. Consequently, for pulse durations in the picosecond range, the primary focusing characteristics are governed by laser ionization, with impact ionization exerting minimal influence.

The difference in plasma generation based on pulse duration is governed by the ratio between laser ionization and impact ionization. Figure 9(a)-(c) depict the normalized laser ionization and impact ionization of oxygen and nitrogen molecules, with normalization anchored to laser ionization of oxygen molecules. Under conditions featuring a pulse duration of 180 fs, impact ionization is minimal, and laser ionization of oxygen dominates the process.

OPTICS CONTINUUM

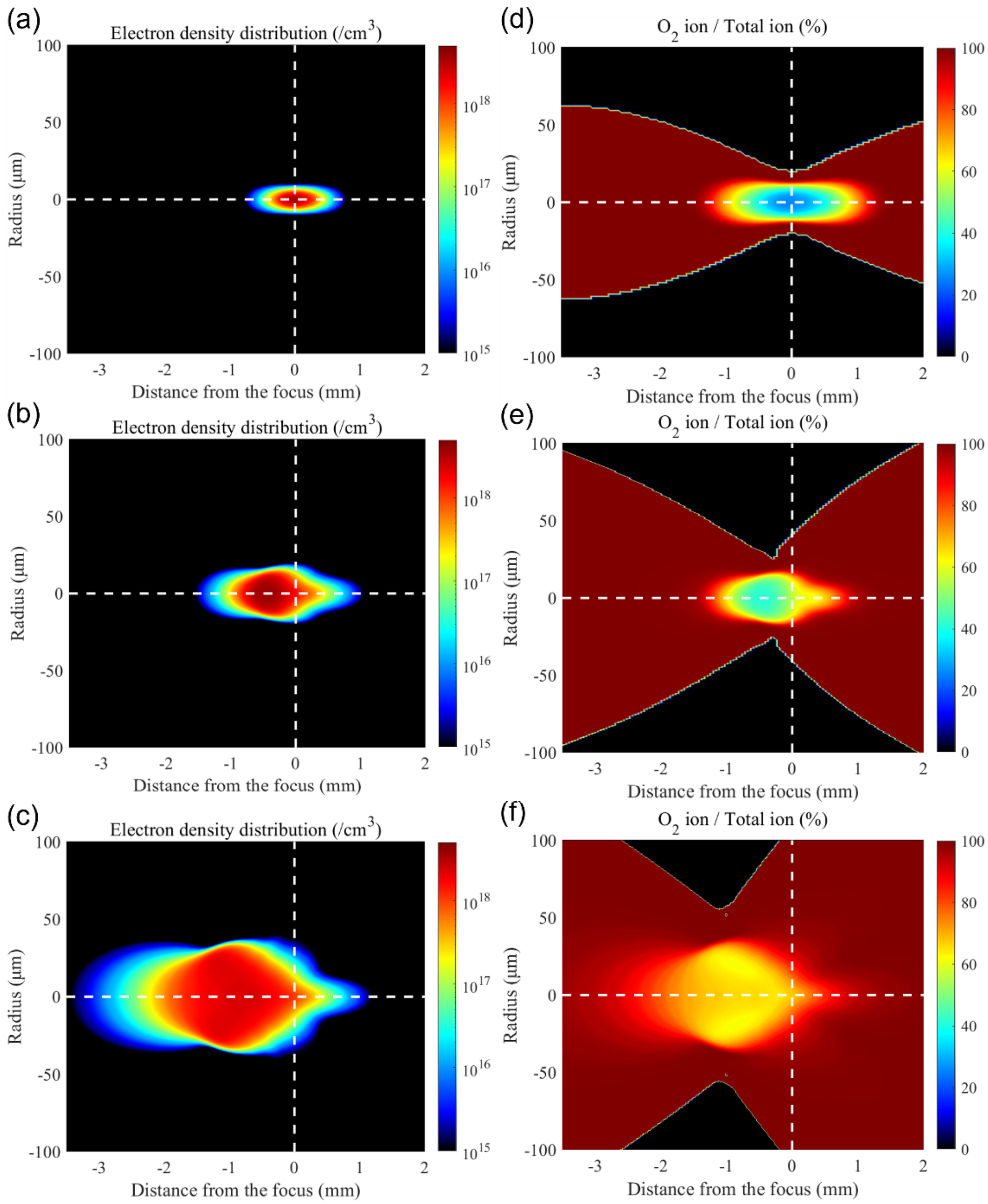

Fig. 8. The free electron density distribution, calculated for varying pulse durations, is illustrated in (a)-(c) with 4 ps, 1 ps, and 180 fs pulse durations, respectively. The proportion of oxygen ions in the total electron density is depicted in (d)-(f) for the same pulse durations.

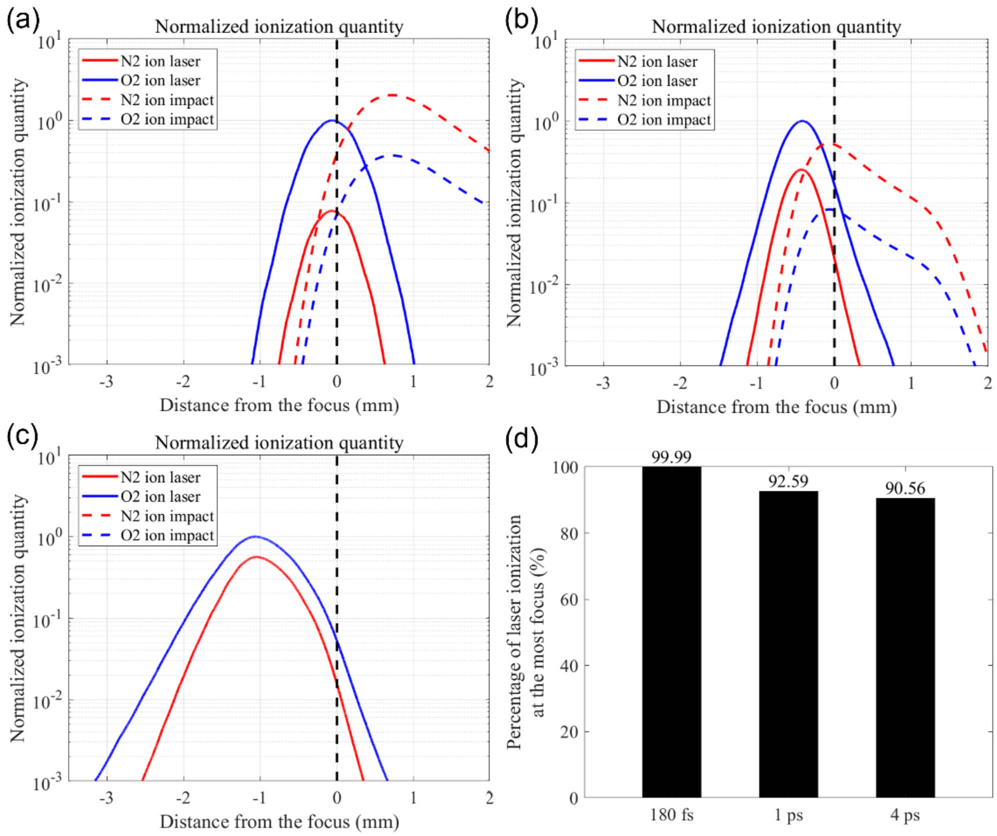

Fig. 9. The amount of ionization per mechanism is quantified for each pulse duration in Figs. 9(a)-(c) for the same pulse durations. (d) Percentage of laser ionization to total ionization at the most focused for each pulse duration.

4. Discussion: nonlinear optical phenomenon

Finally, the contribution of nonlinear optical phenomena under focused conditions, such as those encountered in laser processing, is discussed. It is demonstrated that laser divergence is caused by the plasma, which constrains the laser intensity achieved. This is illustrated through the examination of the amount of phase change per unit propagation length. The equations that encapsulate only the effects of self-focusing caused by the optical Kerr effect and divergence caused by plasma are as follows:

$$\frac{\partial \mathcal{E}}{\partial \xi} = i\frac{k_0}{n_0} n_2 I \mathcal{E} \tag{5}$$

$$\frac{\partial \mathcal{E}}{\partial \xi} = -i\frac{\sigma_{IB}(\omega_0)}{2}\omega_0 \tau_c \rho \mathcal{E} \tag{6}$$

From this, the phase change per unit propagation length can be defined as follows:

$$L_{Kerr} = \frac{k_0}{n_0} n_2 I \tag{7}$$

$$L_{plasma} = -\frac{\sigma_{IB}(\omega_0)}{2}\omega_0 \tau_c \rho \tag{8}$$

OPTICS CONTINUUM

In the case of Gaussian lasers, the center exhibits a higher intensity and electron density; thus, the Kerr effect acts to retard the central phase, while the plasma acts to promote the central phase. Subsequently, the amount of phase change imparted by diffraction is calculated. Transmission through a convex lens is equivalent to imparting the following phase difference to the electric field under initial conditions.

$$\mathcal{E}(z) = \mathcal{E}(z)exp\left(-ik_0\frac{r^2}{2f}\right) \tag{9}$$

By considering the phase difference between the center of the optical axis and the radial position of the beam as representative, it can be observed that the center of the optical axis is phase-lagged relative to the radial position of the beam. As the phase delay at the center of the optical axis is eliminated after propagation through the focal length, the phase change per unit propagation length at the center of the optical axis can be calculated.

$$L_{diffraction} = -k_0\frac{r^2}{2f^2} \tag{10}$$

By comparing the phase change per unit propagation length, the effect of each can be estimated. Under these conditions, the beam radius is set to 1.75 mm and two focal lengths are compared: 70 mm for laser processing (NA = 0.025) and 1 m for laser filamentation (NA = 0.00175). Since there is some correlation between laser intensity and plasma density, we calculated the peak intensity and corresponding plasma density under these conditions. Assuming an ideal Gaussian pulse in the time region of 180 fs, 1 ps, and 4 ps pulse duration, the amount of ionization at various peak intensities up to the center of the pulse was calculated. Given Fig. 9(d), impact ionization can be negligible, since the main cause of the pulse center change is laser ionization. Figure 10(a) shows the plasma density corresponding to the peak intensity. Note that the plasma density is saturated at high laser intensities because only monovalent ionization was considered. Figure 10(b) shows the focusing conditions, the optical Kerr effect corresponding to the peak laser intensity, and the phase change per unit length corresponding to the plasma density at the center of the pulse for each pulse duration. Under low NA focusing conditions, the phase change associated with the optical Kerr effect is greater than that due to diffraction at intensities exceeding 10^{13} W/cm^2. This contributes to self-focusing and creates competition between the plasma and optical Kerr effect. Conversely, under high NA focusing conditions, the phase change of the optical Kerr effect is negligible compared to the phase change due to diffraction and plasma in the range up to 10^{15} W/cm^2. In this case, focusing characteristics are determined only by diffraction and plasma, and the optical Kerr effect does not contribute [19]. The phase change due to diffraction and plasma becomes equal and the phase change of the laser is accelerated when the plasma density reaches 10^{18} /cm^3. This occurs at intensities of 1.0×10^{14} W/cm^2 for 180 fs pulse duration, 7.5×10^{13} W/cm^2 for 1 ps pulse duration, and 6.0×10^{13} W/cm^2 for 4 ps pulse duration. In fact, the saturation laser intensity in the nonlinear propagation calculation is estimated to be 1.5×10^{14} W/cm^2 for 180 fs, 9.3×10^{13} W/cm^2 for 1 ps, and 6.9×10^{13} W/cm^2 for 4 ps, which are commensurate with the estimated intensity. Therefore, the focusing characteristics, including saturation intensity, focusing position, focusing diameter, laser intensity, and fluence distribution, depend on the NA and pulse duration. However, for NA conditions with a phase change larger than the phase change at which the plasma saturates, the saturation intensity is less constrained by plasma defocusing and cannot be estimated, because focusing is more dominant than the effect of plasma defocusing [34]. Based on the above, under conditions of NA < 0.1, the saturation intensity in air can be estimated by the NA and pulse duration, without nonlinear propagation calculations, which helps to understand the focusing characteristics.

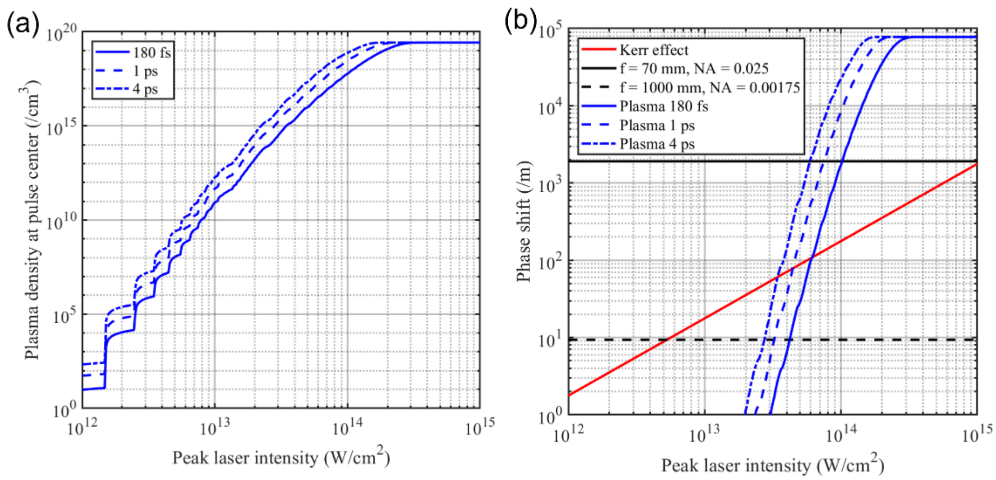

Fig. 10. (a) The amount of plasma generated in relation to the peak laser intensity for each pulse duration. (b) The phase change per unit length for a pulse duration of 180 fs, 1 ps, and 4 ps.

5. Conclusion

In summary, this study simulates the focusing properties of femtosecond to picosecond pulse lasers in laser processing beyond the air ionization threshold and elucidates the role of nonlinear optical phenomena. By visualizing the fluence distribution for each pulse duration, it was demonstrated that the laser diverges upstream under short pulse duration conditions. Specifically, under short pulse duration conditions, the laser is focused upstream, has a larger focusing diameter, and has a lower fluence. The calculated results are in good agreement with the ablation area transition observed in the experiment. Under conditions of high intensity, the efficiency of energy utilization in the process is diminished, necessitating compensation for the laser irradiation position. Nonlinear propagation calculation indicates that the irradiation position can be controlled with sufficient precision. The air ionization is the predominant nonlinear optical phenomenon that governs the focusing characteristics in this condition, with the optical Kerr effect having a negligible effect. Laser ionization of oxygen is primarily responsible for plasma generation, with laser ionization of nitrogen being an order of magnitude smaller. As impact ionization takes several picoseconds after laser ionization, femtosecond pulses are not affected, and even few picoseconds pulses are affected only the weak region of the rear pulse.

Finally, a concise analysis utilizing typical scale lengths demonstrates that the focusing characteristics of lasers under high NA are principally determined by the effects of plasma and diffraction. This results in variations in the irradiated intensity and fluence with NA and pulse duration, and approximations can be obtained. Since it is of utmost importance to judiciously select optimal conditions and consider energy efficiency during laser processing, these findings are fundamental for selecting optimal laser parameters and controlling the laser irradiation position in laser processing areas, where high energy is a requirement.

Appendix: list of terms

E electric field of the laser pulse

I laser intensity, $I = |\mathcal{E}|^2$

τ retarded time in the pulse local frame

k_0 the wave number

n_0 linear refraction index

Γ^{-1} molecular response time

α factor for the proportion of Kerr and Raman-Kerr effects.

$\hbar$ Dirac's constant

ρ_{nt} initial neutral molecule density

σ_{IB} cross section for inverse Bremsstrahlung

U_m ionization potential

ν_m electron impact ionization rate

m electron mass

$\delta(\epsilon)$ Dirac delta function

f focal length

$\mathcal{E}$ envelope of the normalized E

ξ z in a pulse local frame

ω_0 central frequency of the laser pulse

$k_0^{(2)}$ group velocity dispersion

ω_R molecular rotational frequency

K number of photons required for ionization.

W ionization rate

ρ electron density

τ_c electron collision time, $\tau_c = 1/\nu_{cm}$

ϵ electron energy

ν_{cm} electron-neutral collision frequency

e elementary charge

P_m Residual neutral molecule density

Funding. Japan Society for the Promotion of Science (22J10847); Ministry of Education, Culture, Sports, Science and Technology - Quantum Leap Flagship Program (MEXT Q-LEAP) (JPMXS0118068348).

Disclosures. The authors declare no conflicts of interest.

Data availability. Data underlying the results presented in this paper are not publicly available at this time but may be obtained from the authors upon reasonable request.

References

1. B. N. Chichkov, C. Momma, S. Nolte, F. von Alvensleben, and A. Tünnermann, "Femtosecond, picosecond and nanosecond laser ablation of solids," Appl. Phys. A **63**(2), 109–115 (1996).
2. S. Nolte, C. Momma, H. Jacobs, A. Tünnermann, B. N. Chichkov, B. Wellegehausen, and H. Welling, "Ablation of metals by ultrashort laser pulses," J. Opt. Soc. Am. B **14**(10), 2716–2722 (1997).
3. T. Sano, T. Eimura, R. Kashiwabara, T. Matsuda, Y. Isshiki, and A. Hirose, "Femtosecond laser peening of 2024 aluminum alloy without a sacrificial overlay under atmospheric conditions," J. Laser Appl. **29**(1), 012005 (2017).
4. R. Y. Chiao, E. Garmire, and C. H. Townes, "Self-trapping of optical beams," Phys. Rev. Lett. **13**(15), 479–482 (1964).
5. P. Chessa, E. De Wispelaere, F. Dorchies, V. Malka, J. R. Marquès, G. Hamoniauxs, P. Mora, and F. Amiranoff, "Temporal and angular resolution of the ionization-induced refraction of a short laser pulses in helium gas," Phys. Rev. Lett. **82**(3), 552–555 (1999).
6. K. Ishikawa, H. Kumagai, and K. Midorikawa, "High-power regime of femtosecond-laser pulse propagation in silica: multiple-cone formation," Phys. Rev. E **66**(5), 056608 (2002).
7. X. Zhao and Y. C. Shin, "Femtosecond laser ablation of aluminum in vacuum and air at high laser intensity," Appl. Sur. Sci. **283**, 94–99 (2013).
8. C. Pasquier, P. Brandin, R. Clady, N. Sanner, M. Sentis, O. Utéza, Y. Li, and S. Y. Long, "Handling beam propagation in air for nearly 10-fs laser damage experiments," Opt. Commun. **355**, 230–238 (2015).
9. C. Pasquier, M. Sentis, O. Utéza, and N. Sanner, "Predictable surface ablation of dielectrics with few-cycle laser pulse even beyond air ionization," Appl. Phys. Lett. **109**(5), 051102 (2016).
10. I. Nishibata, M. Yoshida, Y. Ito, N. Sugita, A. Hirose, and T. Sano, "Pulse duration dependence of dry laser peening effects in the femtosecond-to-picosecond regime," Appl. Phys. Express **14**(6), 062001 (2021).
11. A. Couairon, E. Brambilla, T. Corti, D. Majus, O. d. J. Ramirez-Góngora, and M. Kolesik, "Practitioner's guide to laser pulse propagation models and simulation," Eur. Phys. J. Spec. Top. **199**(1), 5–76 (2011).
12. M. Kolesik and J. V. Moloner, "Modeling and simulation techniques in extreme nonlinear optics of gaseous and condensed media," Rep. Prog. Phys. **77**(1), 016401 (2014).
13. L. V. Keldysh, "Ionization in the field of a strong electromagnetic wave," Sov. Phys. JETP **20**(5), 1307–1314 (1965).
14. A. M. Perelomov, V. S. Popov, and M. V. Terent'ev, "Ionization of atoms in an alternating electric field," Sov. Phys. JETP **23**(5), 924–934 (1966).
15. S. L. Chin, S. A. Hosseini, W. Liu, Q. Luo, F. Théberge, N. Aközbek, A. Becker, V. P. Lamdodpv, O. G. Kosareva, and H. Shroeder, "The propagation of powerful femtosecond laser pulses in optical media: physics, applications, and new challenges," Can. J. Phys. **83**(9), 863–905 (2005).
16. L. Bergé, S. Skupin, R. Nuter, J. Kasparian, and J.-P. Wolf, "Ultrashort filaments of light in weakly ionized, optically transparent media," Rep. Prog. Phys. **70**(10), 1633–1713 (2007).
17. A. Couairon and A. Mysyrowicz, "Femtosecond filamentation in transparent media," Phys. Rep. **441**(2-4), 47–189 (2007).
18. S. L. Chin, T.-J. Wang, C. Marceau, J. Wu, J. S. Liu, O. Kosareva, N. Panov, Y. P. Chen, J.-F. Daigle, S. Yuan, A. Azarm, W. W. Liu, T. Seideman, H. P. Zeng, M. Richardsono, R. Li, and Z. Z. Xu, "Advances in intense femtosecond laser filamentation in air," Laser Phys. **22**(1), 1–53 (2012).
19. F. Théberge, W. Liu, P. T. Simard, A. Becker, and S. L. Chin, "Plasma density inside a femtosecond laser filament in air: strong dependence on external focusing," Phys. Rev. E **74**(3), 036406 (2006).
20. Y. T. Li, T. T. Xi, Z. Q. Hao, Z. Zhang, X. Y. Peng, K. Li, Z. Jin, Z. Y. Zheng, Q. Z. Yu, X. Lu, and J. Zhang, "Oval-like hollow intensity distribution of tightly focused femtosecond laser pulses in air," Opt. Express **15**(26), 17973–17979 (2007).
21. Y. E. Geints, D. V. Mokrousova, D. V. Pushkarev, G. E. Rizaev, L. V. Seleznev, I. Y. Geints, A. A. Ionin, and A. A. Zemlyanov, "Energy limit for linear-to-nonlinear femtosecond laser pulse focusing in air," Opt. Laser Technol. **143**, 107377 (2021).
22. A. Schmitt-Sody, H. G. Kurz, L. Bergé, S. Skupin, and P. Polynkin, "Picosecond laser filamentation in air," New J. Phys. **18**(9), 093005 (2016).
23. J. K. Koga, K. Moribayashi, Y. Fukuda, S. V. Bulanov, A. Sagisaka, K. Ogura, H. Daido, M. Yamagiwa, T. Kimura, T. Fujikawa, M. Ebina, and K. Akihama, "Simulation and experiments of the laser induced breakdown of air for femtosecond to nanosecond order pulses," J. Phys. D: Appl. Phys. **43**(2), 025204 (2010).
24. J. Sun and J. P. Longtin, "Effects of a gas medium on ultrafast laser beam delivery and materials processing," J. Opt. Soc. Am. B **21**(5), 1081–1088 (2004).
25. S. R. Vatsya, C. Li, and S. K. Nikumb, "Surface profile of material ablated with high-power lasers in ambient air medium," J. Appl. Phys. (Melville, NY, U. S.) **97**(3), 034912 (2005).
26. C. Li, S. R. Vatsya, and S. K. Nikumb, "Effect of plasma on ultrashort pulse laser material processing," J. Laser Appl. **19**(1), 26–31 (2007).
27. R. Yamada, W. Komatsubara, H. Sakurai, K. Konishi, N. Mio, J. Yumoto, and M. Kuwata-Gonokami, "Simulation of nonlinear propagation of femtosecond laser pulses in air for quantitative prediction of the ablation crater shape," Opt. Express **31**(5), 7363–7382 (2023).
28. C. Tian and C. R. Vidal, "Electron impact ionization of N_2 and O_2: contributions from different dissociation channels of multiply ionized molecules," J. Phys. B: At. Mol. Opt. Phys. **31**(24), 5369–5381 (1998).

OPTICS CONTINUUM

29. A. Talebpour, J. Yang, and S. L. Chin, "Semi-empirical model for the rate of tunnel ionization of N_2 and O_2 molecule in an intense Ti:sapphire laser pulses," Opt. Commun. **163**(1-3), 29–32 (1999).
30. S. Zahedpour, J. K. Wahlstrand, and H. M. Milchberg, "Measurement of the nonlinear refractive index of air constituent at mid-infrared wavelengths," Opt. Lett. **40**(24), 5794–5797 (2015).
31. E. T. J. Nibbering, G. Grillon, M. A. Franco, B. S. Prade, and A. Mysyrowicz, "Determination of the inertial contribution to the nonlinear refractive index of air, N_2, and O_2 by use of unfocused high-intensity femtosecond laser pulses," J. Opt. Soc. Am. B **14**(3), 650–660 (1997).
32. P. J. Wrzesinski, D. Pestov, V. V. Lozovoy, J. R. Gord, M. Dantus, and S. Roy, "Group-velocity-dispersion measurements of atmospheric and combustion-related gases using an ultrabroadband-laser source," Opt. Express **19**(6), 5163–5170 (2011).
33. N. Zhang, W. Wang, X. Zhu, J. Liu, K. Xu, P. Huang, J. Zhao, R. Li, and M. Wang, "Investigation of ultrashort pulse laser ablation of solid targets by measuring the ablation-generated momentum using a torsion pendulum," Opt. Express **19**(9), 8870–8878 (2011).
34. P. Prem Kiran, S. Baguchi, S. R. Krishnan, C. L. Arnold, G. R. Kumar, and A. Couairon, "Focal dynamics of multiple filaments: microscopic imaging and reconstruction," Phys. Rev. A **82**(1), 013805 (2010).